Supplemental Note

Isometric geodesic theory

In GeoBridge, we first obtain a geodesic in the latent space manifold as a constant-velocity straight line via linear interpolation. These interpolated points are then mapped back to the original space through the inverse mapping of the GeoBridge to obtain their corresponding trajectories in the original manifold. However, such trajectories are not necessarily geodesics in the original manifold. We further proved that if the diffeomorphism(GeoBridge's INN model) between two manifolds is a local isometry, then there exists a one-to-one correspondence between their geodesic curves.

- Lemma for Components of the Pullback of a Metric Tensor: Let M and N be two smooth manifolds, with a smooth mapping $\phi: M \to N$. Suppose N carries a metric tensor g_{ab} with local components $g_{\mu\nu}$. We aim to compute the components of the pullback metric tensor $(\phi^* g)_{ab}$.

Consider a tangent vector $v^a \in TM$. Let $\{x^\mu\}$ and $\{y^\nu\}$ be local coordinate systems on M and N, respectively. For the coordinate basis vector $\frac{\partial}{\partial x^\mu}$, and any scalar field f on N, the definition of the pushforward gives:

$$\left(\phi_* \frac{\partial}{\partial x^\mu}\right)(f) = \frac{\partial}{\partial x^\mu}(\phi^* f) = \frac{\partial f(y)}{\partial x^\mu} = \frac{\partial y^\nu}{\partial x^\mu}\frac{\partial f}{\partial y^\nu} \tag{1}$$

Since f is arbitrary, one has:

$$\left(\phi_* \frac{\partial}{\partial x^\mu}\right)^a = \frac{\partial y^\nu}{\partial x^\mu}\left(\frac{\partial}{\partial y^\nu}\right)^a \tag{2}$$

Now, for the pullback metric, by definition:

$$(\phi^* g_{ab}) v^a u^b = g_{ab}(\phi_* v)^a (\phi_* u)^b = g_{\mu\nu}\frac{\partial y^\mu}{\partial x^\rho} v^\rho \frac{\partial y^\nu}{\partial x^\sigma} u^\sigma \tag{3}$$

Since v^a, u^b are arbitrary, it follows that:

$$(\phi^* g)_{ab} = g_{\mu\nu}\frac{\partial y^\mu}{\partial x^\rho}(\mathrm{d}x^\rho)_a \frac{\partial y^\nu}{\partial x^\sigma}(\mathrm{d}x^\sigma)_b \tag{4}$$

Then, we can prove our main theoretical results: Theorems 1 and 2 of bijective diffeomorphism and geodesic bridge theory, which ensure local isometric projects.

-Theorem 1 : Let (M, g'_{ab}) and (N, g_{ab}) be two Riemannian manifolds, and $\phi: M \to N$ a smooth mapping. If, for any two sufficiently close points $x, y \in M$, the geodesic distances satisfy

$$D_M(x, y) = D_N\big(\phi(x), \phi(y)\big) \tag{5}$$

then

$$g'_{ab} = (\phi^* g)_{ab} \tag{6}$$

Proof:

Choose local coordinates $\{x^\mu\}$ on M and $\{y^\nu\}$ on N. Since condition 1 holds for any two sufficiently close points $p, q \in M$, take p, q with small coordinate difference $v^\mu = x_2^\mu - x_1^\mu$.

Using the first-order expansion of the geodesic distance in M:

$$D_M(p,q) = g'_{\mu\nu} v^\mu v^\nu \tag{7}$$

For the image points under ϕ, the coordinate difference is:

$$u^\mu = y_2^\mu - y_1^\mu = \frac{\partial y^\mu}{\partial x^\nu} v^\nu \tag{8}$$

Thus in N:

$$D_N\big(\phi(p), \phi(q)\big) = g_{\mu\nu} u^\mu u^\nu = g_{\mu\nu} \frac{\partial y^\mu}{\partial x^\rho} v^\rho \frac{\partial y^\nu}{\partial x^\sigma} v^\sigma \tag{9}$$

By the given condition $D^M(p,q) = D^N(\phi(p), \phi(q))$, we identify:

$$g'_{\rho\sigma} = g_{\mu\nu} \frac{\partial y^\mu}{\partial x^\rho} \frac{\partial y^\nu}{\partial x^\sigma} \tag{10}$$

which is precisely the pullback metric $(\phi^* g)_{\rho\sigma}$. ■

Then, we have our geodesic bridge theorem next, which is the theoretical basis of this work.

-Theorem 2: Let (M, g'_{ab}) and (N, g_{ab}) be Riemannian manifolds, with a smooth mapping $\phi: M \to N$. If $\gamma(t)$ is a geodesic in N with respect to g_{ab}, then its pullback curve $\phi^{-1}(\gamma(t))$ (assuming it exists) is a geodesic in M with respect to $g'_{ab} = (\phi^* g)_{ab}$.

Proof:

Let ∇_a be the torsion-free, metric-compatible connection on N associated with g_{ab}. Define ∇'_a on M via:

$$\nabla'_a T^{b_1 \cdots b_k}{}_{c_1 \cdots c_l} = \phi^*\big(\nabla_a (\phi_* T)\big)^{b_1 \cdots b_k}{}_{c_1 \cdots c_l} \tag{11}$$

First, we verify ∇'_a is torsion-free. For any vector fields u'^a, v'^a on M, with pushforwards u^a, v^a on N, the torsion tensor is:

$$T'^c{}_{ab} u'^a v'^b = u'^a \nabla'_a v'^c - v'^a \nabla'_a u'^c - [u', v']^c \tag{12}$$

By construction of ∇'_a and the compatibility of pushforward/pullback with tensor products and Lie brackets, we have:

$$T'^c{}_{ab} u'^a v'^b = \phi^*(u^a \nabla_a v^c - v^a \nabla_a u^c - [u, v]^c) = 0 \tag{13}$$

since ∇_a is torsion-free.

Second, ∇'_a is metric-compatible:

$$\nabla'_a g'_{bc} = \phi^*(\nabla_a g_{bc}) = 0 \tag{14}$$

Now, let T^a be the tangent vector to a geodesic $\gamma(t)$ in N, satisfying $T^b\nabla_b T^a = 0$. Let T'^a be the pullback of T^a to M. Then:

$$T'^b\nabla'_b T'^a = \phi^*\left((\phi_* T'^b)\nabla_b(\phi_* T')^a\right) = \phi^*(T^b\nabla_b T^a) = 0 \tag{15}$$

showing that the pullback curve in M is also a geodesic. ■

(See, e.g., Liang can bin, Differential Geometry and General Relativity , Vol. 1, 2nd ed)

Supplemental Information

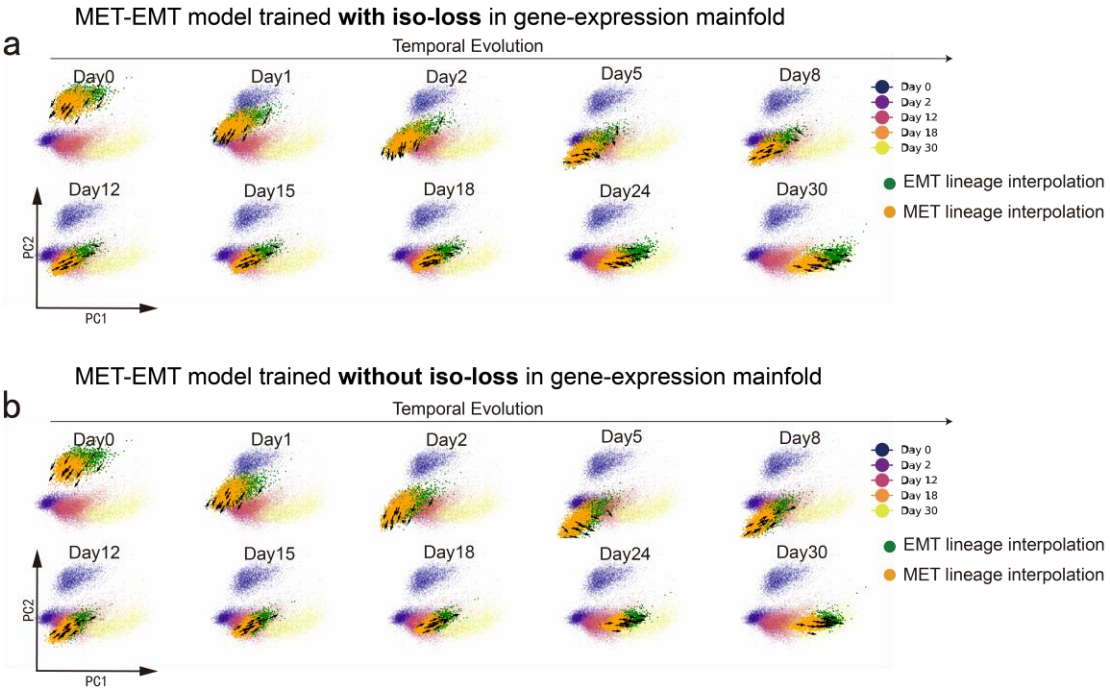

Supplementary Figure S1 | Ablation study on the effect of the isometric loss. a, Reconstruction of intermediate cellular states in the gene-expression manifold generated by a model trained with the isometric loss. **b**, Reconstruction of intermediate cellular states in the gene-expression manifold generated by a model trained without the isometric loss. The results show that models without the isometric loss produce interpolations that deviate substantially from the original data manifold, particularly at day 5 and day 8 as illustrated.

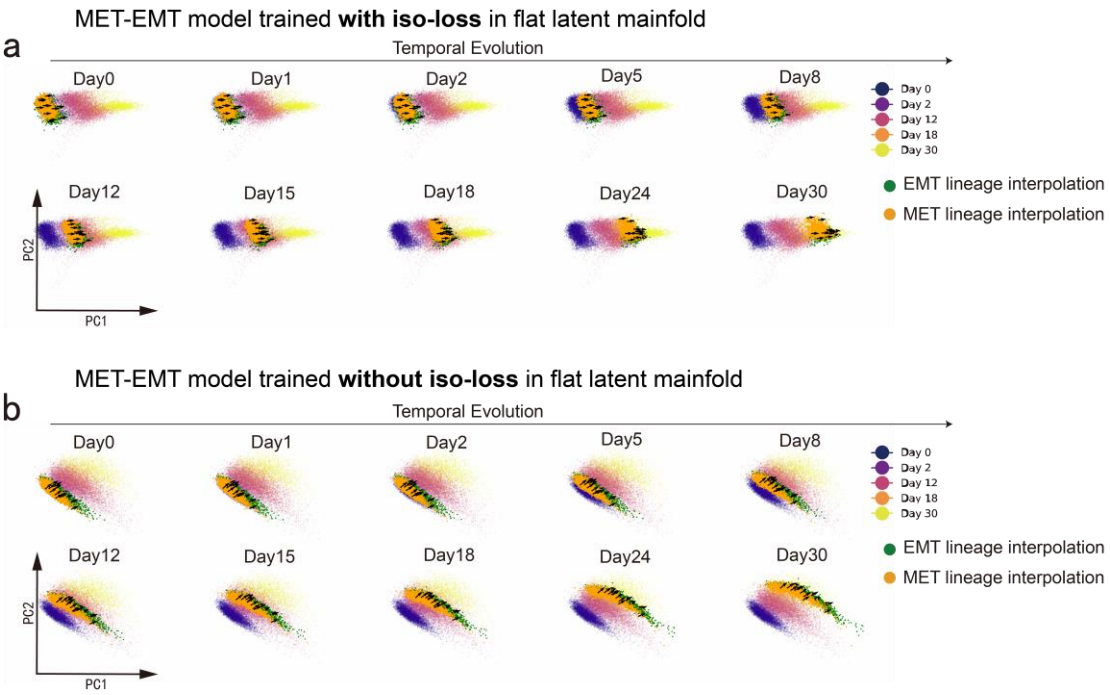

Supplementary Figure S2 | Ablation study on the effect of the isometric loss in the flat latent manifold. a, Reconstruction of intermediate cellular states in the flat latent manifold generated by a model trained with the isometric loss. **b**, Reconstruction of intermediate cellular states in the flat latent manifold generated by a model trained without the isometric loss. Both models produce interpolations that do not visibly deviate from the original data manifold in the flat latent space, indicating that a constant-velocity linear loss alone can yield a flat latent manifold geometry. However, without the isometric loss, straight geodesics in the latent space can be inversely mapped back to paths that are not geodesics on the original data manifold, potentially causing deviations from the true manifold in the original space.

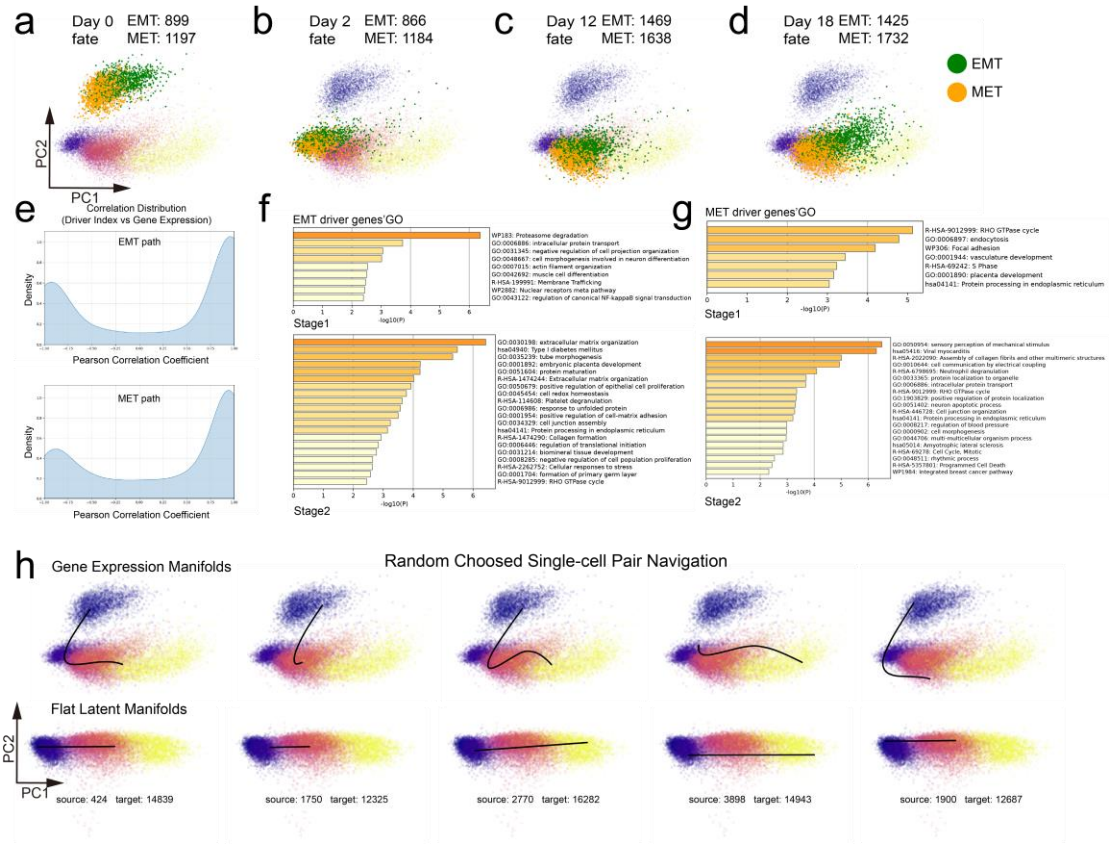

Supplementary Figure S3 | Additional results of GeoBridge for EMT and MET progression datasets. **a-d,** Cell fate determination results of individual cells in undifferentiated annotated cancer stem cells at day 0, day 2, day 12, and day 18. **e**, Pearson correlation coefficient between the gene dynamic driver index and gene dynamic expression over temporal evolution. **f-g**, EMT and MET Top 100 driver genes' GO analysis from metascape. **h**, Navigation trajectories for randomly choosed single-cell pairs, showing geodesic paths between two cells (top: gene expression manifold; bottom: flat latent space). Source and Target at the bottom indicate the indices of the two cells within the dataset.

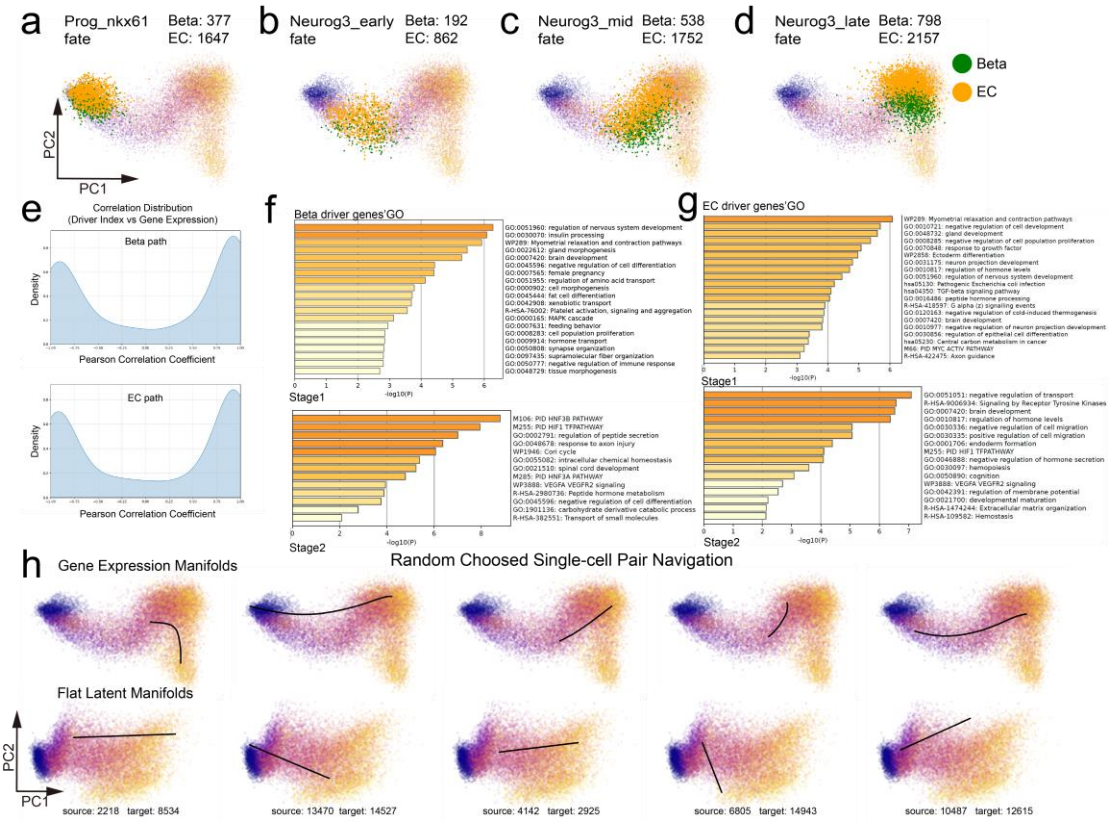

Supplementary Figure S4 | Additional results of GeoBridge for pancreatic endocrine lineages datasets. a-d, Cell fate determination results of individual cells in undifferentiated annotated HPSCs at Prog_NKX6.1, NEUROG3_early, NEUROG3_mid, and NEUROG3_late stage. **e**, Pearson correlation coefficient between the gene dynamic driver index and gene dynamic expression over temporal evolution. **f-g**, Beta and EC path Top 100 driver genes' GO analysis from metascape. **h**, Navigation trajectories for randomly choosed single-cell pairs, showing geodesic paths between two cells (top: gene expression manifold; bottom: flat latent space). Source and Target at the bottom indicate the indices of the two cells within the dataset.

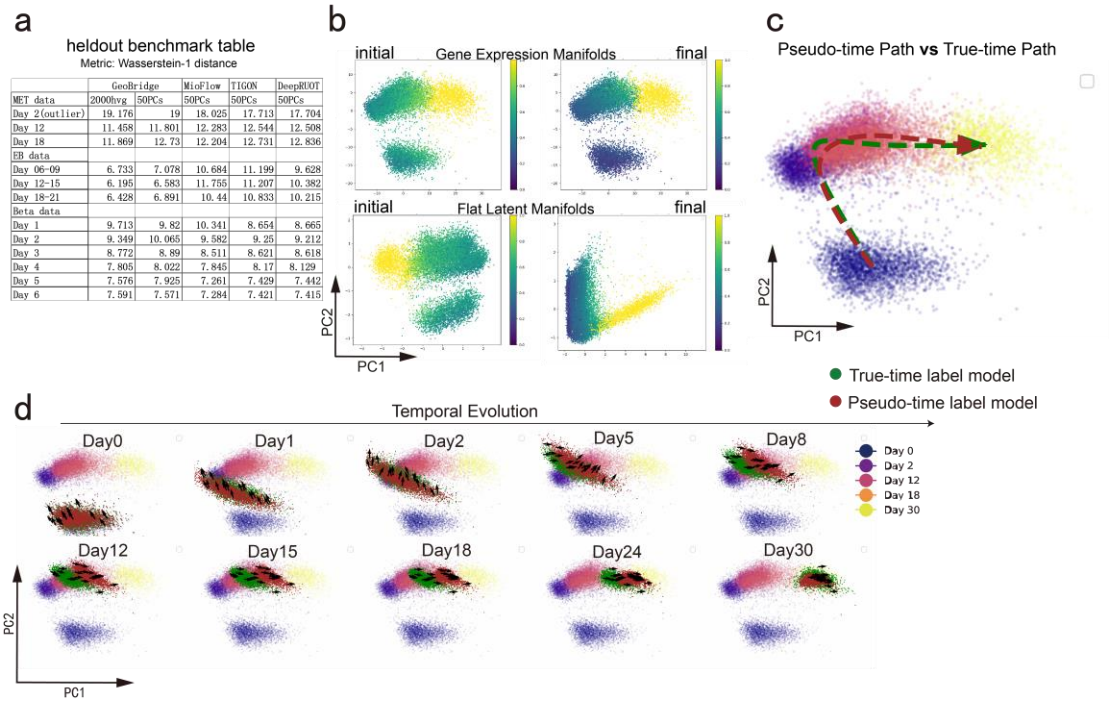

	GeoBridge		MioFlow	TIGON	DeepRUOT
MET data	2000hvg	50PCs	50PCs	50PCs	50PCs
Day 2(outlier)	19.176	19	18.025	17.713	17.704
Day 12	11.458	11.801	12.283	12.544	12.508
Day 18	11.869	12.73	12.204	12.731	12.836
EB data					
Day 06-09	6.733	7.078	10.684	11.199	9.628
Day 12-15	6.195	6.583	11.755	11.207	10.382
Day 18-21	6.428	6.891	10.44	10.833	10.215
Beta data					
Day 1	9.713	9.82	10.341	8.654	8.665
Day 2	9.349	10.065	9.582	9.25	9.212
Day 3	8.772	8.89	8.511	8.621	8.618
Day 4	7.805	8.022	7.845	8.17	8.129
Day 5	7.576	7.925	7.261	7.429	7.442
Day 6	7.591	7.571	7.284	7.421	7.415

Supplementary Figure S5 | Additional results of GeoBridge for heldout and pseudotime benchmarking. a, Heldout results of four methods—GeoBridge, MioFlow, TIGON, and DeepRUOT—across three datasets. **b**, Initial and final pseudo-time inference results obtained through iterative updating in GeoBridge. **c**, Average trajectories constructed by GeoBridge using true-time label and iterative updated pseudotime label. **d**, Reconstruction of intermediate cellular states in the gene-expression manifold by true-time label model and pseudotime label model. The arrows indicate the velocities of ten randomly selected cells from each lineage. **c-d** Comparison of reconstructed continuous cellular dynamics, showing that a model trained with pseudotime labels achieves results highly similar to one trained with ground-truth experimental time labels.

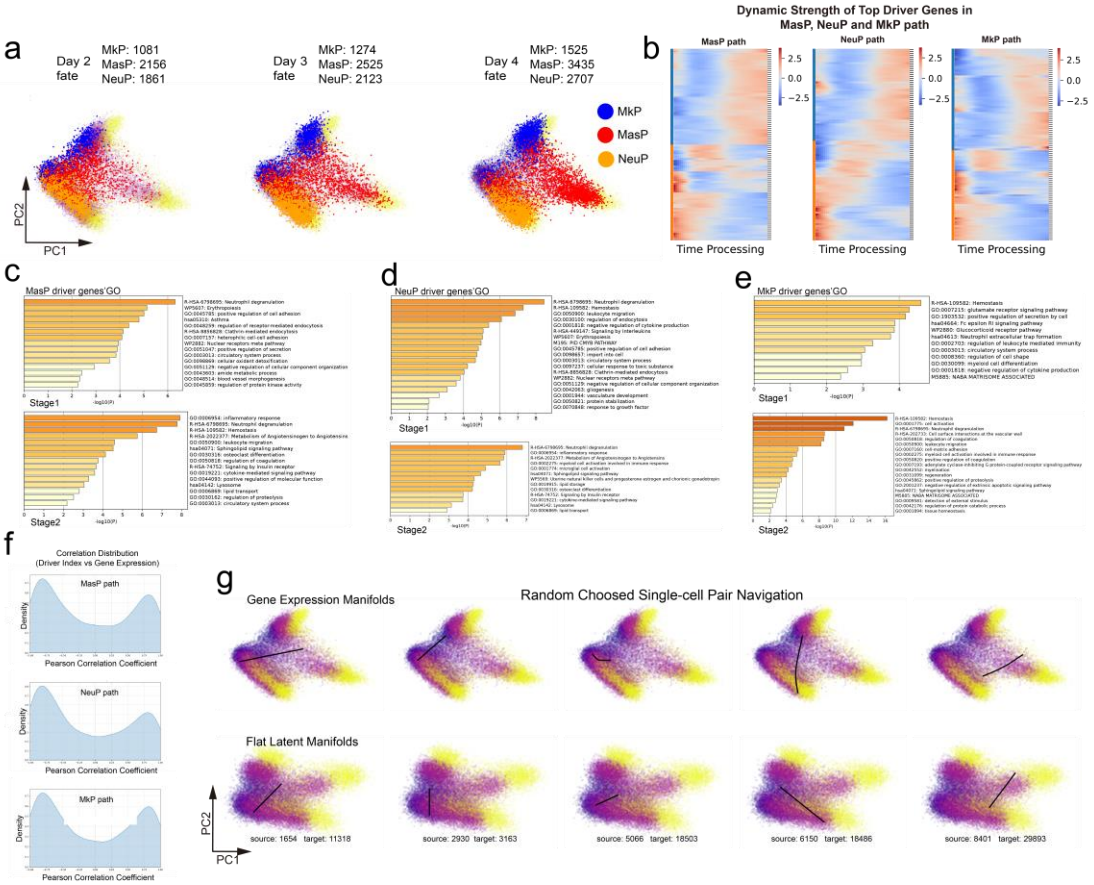

Supplementary Figure S6 | Additional results of GeoBridge for multi target hematopoietic lineages datasets. a, Cell fate determination results of individual cells in undifferentiated annotated HPSCs at day2, day3, and day4. b, Heatmap of Top 100 dynamic driver indices highlighting temporally distinct regulatory modules along MasP, NeuP, and MkP lineages. **c-e**, MasP, NeuP, and MkP path Top 100 driver genes' GO analysis from metascape. **f**, Pearson correlation coefficient between the gene dynamic driver index and gene dynamic expression over temporal evolution. **g**, Navigation trajectories for random choosed single-cell pairs, showing geodesic paths between two cells (top: gene expression manifold; bottom: flat latent space). Source and Target at the bottom indicate the indices of the two cells within the dataset.

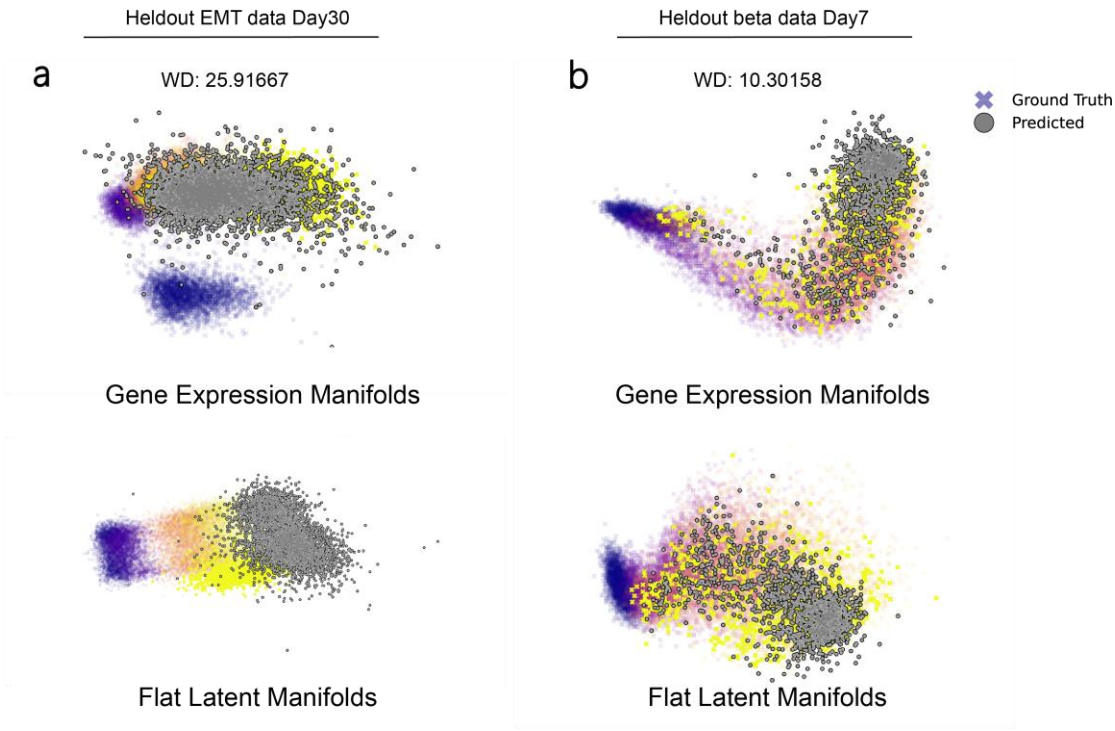

Supplementary Figure S7 | Held-out prediction results for future time points of 2000hvgs. a, Example from EMT dataset at day 30, where future state changes involve a pronounced deviation from prior trajectories, resulting in poorer prediction performance. **b**, Example from beta dataset at day 7, where future changes follow the existing trend with limited nonlinearity, leading to more accurate predictions.

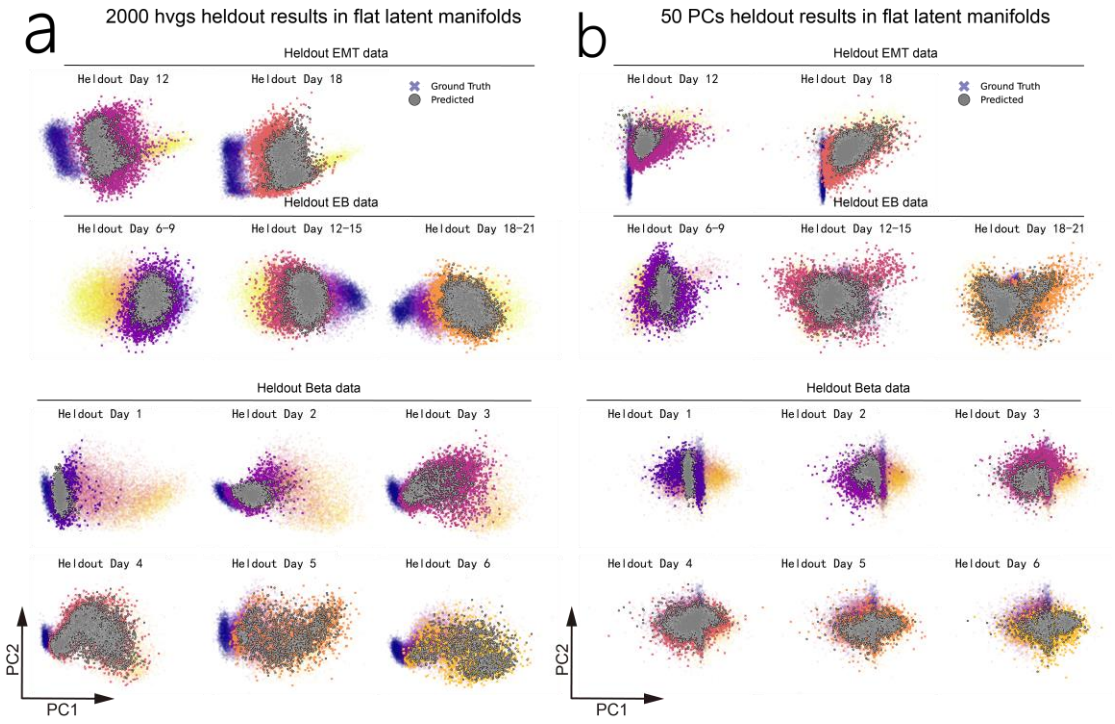

Supplementary Figure S8 | Heldout interpolation results in flat latent results. a-b, 2000 hvgs and 50 PCs heldout interpolation results visualized in the latent space of EMT, EB, and β-cell datasets.

Generated points are highly overlapping with the ground truth, consistent with the corresponding visualizations on the gene expression manifold.

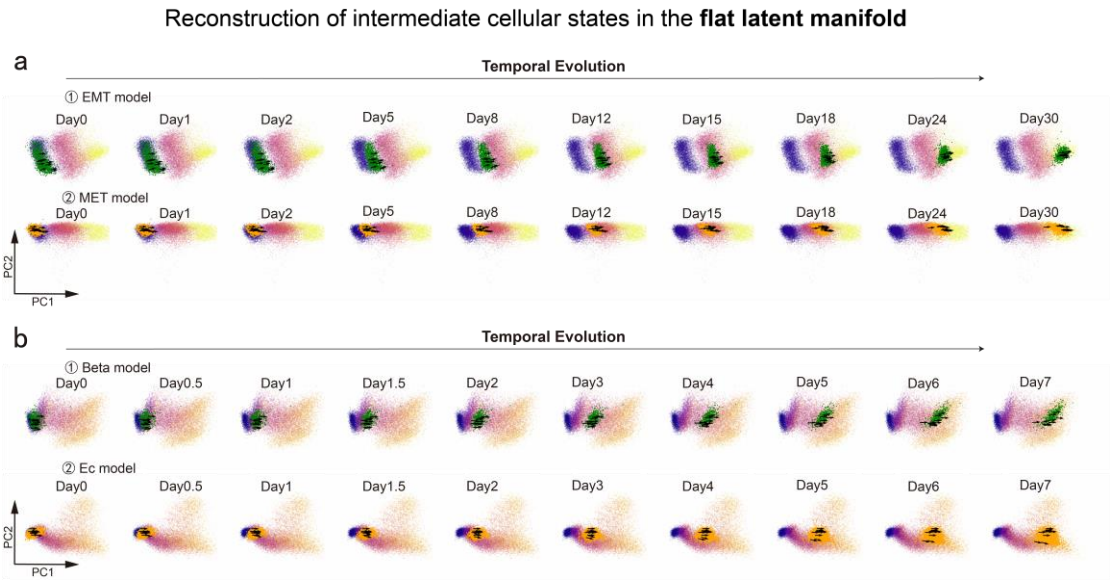

Supplementary Figure S9 | Additional results of GeoBridge for reconstructing intermediate cellular states in the flat latent manifold. a, Latent space dynamic interpolation along EMT and MET paths. **b,** Latent space dynamic interpolation along Beta and Ec paths. The arrows indicate the velocities of ten randomly selected cells from each lineage. The constant direction of the velocity vectors demonstrates uniform straight-line geodesics in the latent space.

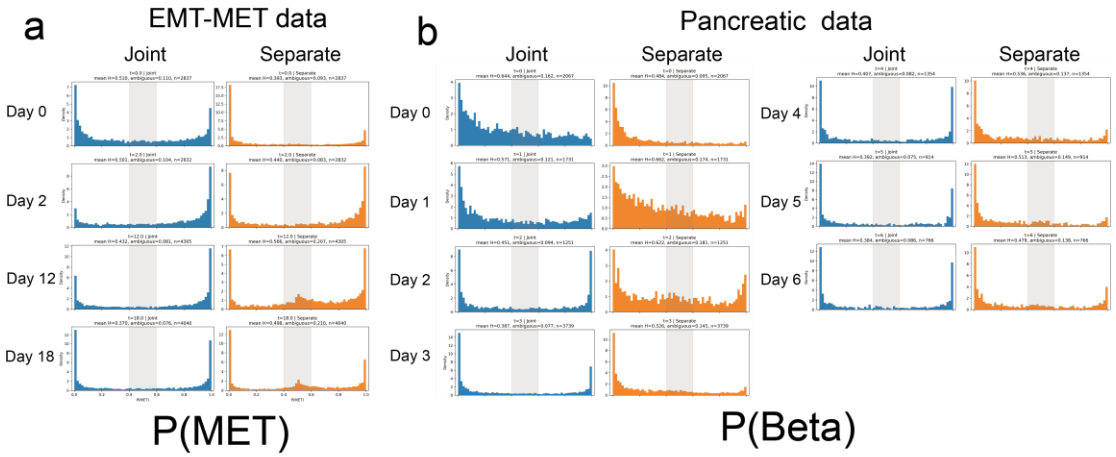

c

Summary table

Dataset	Time	Mean entropy (Joint)	Mean entropy (Separate	Ambiguous (Joint)	Ambiguous (Separate)
MET_EMT	0.0	0.510	0.393	0.110	0.093
MET_EMT	2.0	0.501	0.440	0.104	0.083
MET_EMT	12.0	0.432	0.566	0.081	0.207
MET_EMT	18.0	0.370	0.498	0.076	0.210
Beta_Ec	0	0.646	0.488	0.158	0.095
Beta_Ec	1	0.572	0.667	0.120	0.180
Beta_Ec	2	0.451	0.628	0.096	0.189
Beta_Ec	3	0.387	0.530	0.079	0.144
Beta_Ec	4	0.408	0.540	0.080	0.142
Beta_Ec	5	0.392	0.518	0.078	0.150
Beta_Ec	6	0.383	0.485	0.090	0.145

Supplementary Figure S10 | Comparison of fate-prediction certainty between separate and joint training. a, b, Histograms of predicted fate probabilities across time points for the EMT–MET dataset. **a,** and the pancreatic Beta–Ec dataset. **b,** under joint and separate training. The x-axes show P(MET) for the EMT–MET dataset and P(Beta) for the pancreatic dataset. Blue and orange histograms correspond to joint and separate training, respectively. The gray shaded region marks the ambiguous probability interval, where cells have similar probabilities for alternative terminal fates and therefore cannot be confidently assigned to one fate. **c,** Summary table comparing mean entropy and ambiguous-cell fraction between joint and separate training. Joint training generally resulted in lower entropy and fewer ambiguous cells at later time points in both datasets, supporting its advantage for competitive multi-fate allocation.

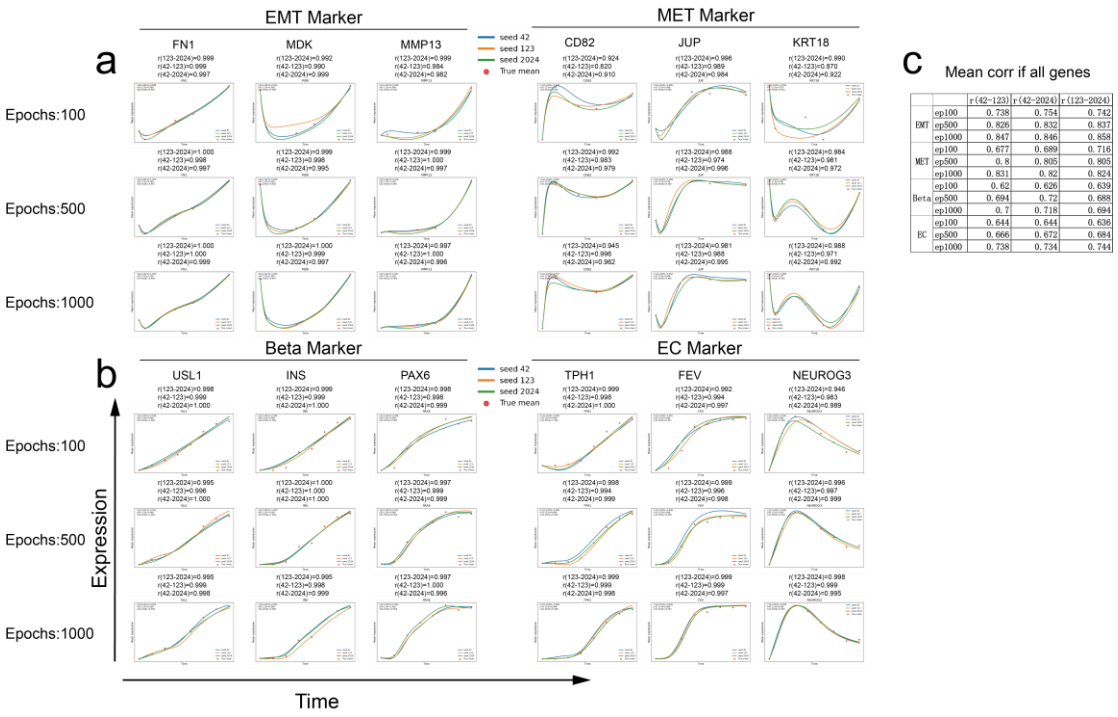

		r(42-123)	r(42-2024)	r(123-2024)
EMT	ep100	0.738	0.754	0.742
	ep500	0.826	0.832	0.837
	ep1000	0.847	0.846	0.858
MET	ep100	0.677	0.689	0.716
	ep500	0.8	0.805	0.805
	ep1000	0.831	0.82	0.824
Beta	ep100	0.62	0.626	0.639
	ep500	0.694	0.72	0.688
	ep1000	0.7	0.718	0.694
EC	ep100	0.644	0.644	0.636
	ep500	0.666	0.672	0.684
	ep1000	0.738	0.734	0.744

Supplementary Figure S11 | Robustness of gene expression dynamics across random seeds. a–b, Representative dynamic expression trajectories of key marker genes along the interpolated trajectory, inferred under three random seeds (42, 123, 2024; colored curves). Red dots denote the mean expression of real data at each time point. Pairwise Pearson correlations (r) between seeds are annotated in each panel. **c,** Mean Pearson correlation of dynamic expression profiles across all genes, computed for each seed pair in each dataset and epoch condition. Values represent the average per-gene time-course correlation. Results are shown for four datasets (EMT, MET, sc-beta, sc-ec) across three training configurations (epochs 100, 500, 1000).

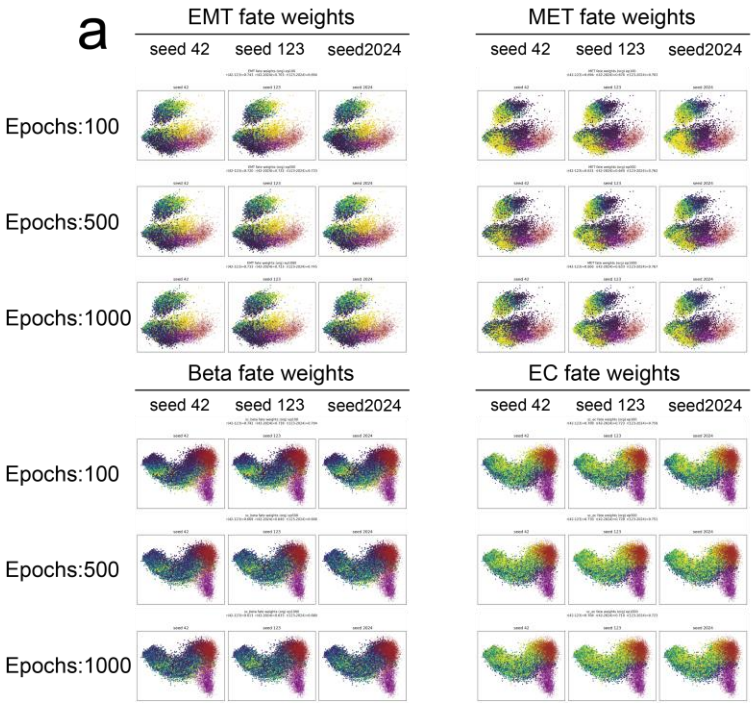

b

Corr of cell fate weights

		r(42-123)	r(42-2024)	r(123-2024)
EMT	ep100	0.743130919	0.702953896	0.693722348
	ep500	0.719811188	0.732218158	0.732771713
	ep1000	0.73266816	0.723245485	0.745014095
MET	ep100	0.694339151	0.676462995	0.70288128
	ep500	0.631172132	0.640451678	0.761760603
	ep1000	0.606325323	0.633023641	0.766596283
Beta	ep100	0.741707296	0.738844809	0.704091675
	ep500	0.668926601	0.640157532	0.605507544
	ep1000	0.613052281	0.633111092	0.680001389
EC	ep100	0.708739245	0.722778237	0.758941851
	ep500	0.729577151	0.728081964	0.75051677
	ep1000	0.703667224	0.709506767	0.7230898

Supplementary Figure S12 | Robustness of cell fate weight predictions across random seeds. a, Spatial distribution of predicted fate weights visualized on the original expression space (PCA), colored by the continuous probability of each cell differentiating toward the indicated target fate. Three columns correspond to three random seeds (42, 123, 2024). **b,** Pearson correlation of cell fate weights between seed pairs, computed across all cells for each target fate, dataset, and epoch configuration. Results are shown for EMT/MET and sc-beta/sc-ec datasets under three epoch settings (100, 500, 1000).

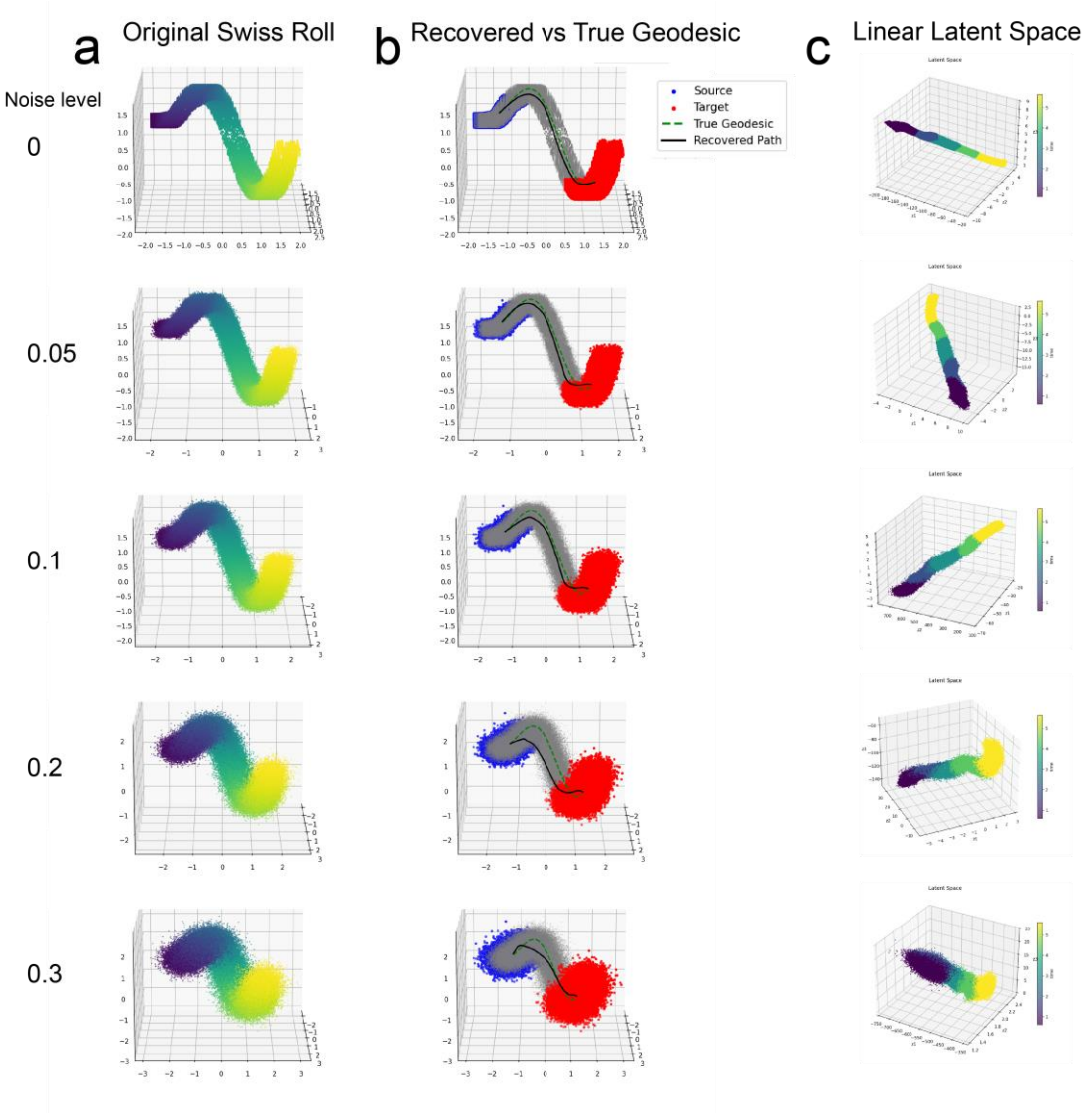

Supplementary Figure S12 | Performance of the INN model across different spatial noise levels (0.0, 0.05, 0.1, 0.2, and 0.3). **a,** The input 3D Swiss Roll manifold with thickness, colored by their discrete temporal bins. **b,** Comparison between the analytical true geodesic (green dashed line) and the recovered geodesic path (black solid line) mapped back to the original ambient space. The source and target regions are highlighted in blue and red, respectively. **c,** The learned latent space representations. The INN successfully "unrolls" the complex, folded manifold into a straightened, linear structure in the latent space.

		Pearson			Jaccard			Top20_TC		
dataset	epoch	42-123	42-2024	123-2024	42-123	42-2024	123-2024	42-123	42-2024	123-2024
EMT	ep100	0.699	0.495	0.436	0.258	0.25	0.227	0.507	0.481	0.513
	ep500	0.785	0.706	0.639	0.266	0.235	0.235	0.506	0.489	0.417
	ep1000	0.774	0.723	0.731	0.227	0.212	0.242	0.514	0.443	0.442
MET	ep100	0.751	0.732	0.733	0.22	0.235	0.29	0.472	0.451	0.507
	ep500	0.774	0.748	0.768	0.235	0.29	0.307	0.532	0.506	0.508
	ep1000	0.803	0.722	0.765	0.25	0.205	0.307	0.518	0.51	0.545
Beta	ep100	0.858	0.933	0.86	0.471	0.538	0.46	0.329	0.325	0.307
	ep500	0.897	0.908	0.907	0.408	0.429	0.399	0.446	0.456	0.481
	ep1000	0.861	0.869	0.89	0.379	0.333	0.361	0.44	0.47	0.422
EC	ep100	0.897	0.9	0.901	0.46	0.439	0.481	0.463	0.441	0.375
	ep500	0.879	0.876	0.918	0.399	0.361	0.418	0.445	0.456	0.424
	ep1000	0.852	0.873	0.896	0.351	0.333	0.316	0.457	0.496	0.445

Supplementary Table S1 | Cross-seed reproducibility of driver gene identification. Driver scores computed under three random seeds (42, 123, 2024) for each dataset and epoch configuration. Three metrics are reported for each seed pair: Pearson correlation of time-averaged driver scores (global ranking reproducibility), Jaccard overlap of the top-100 driver genes, and mean time-course correlation within the top-20% strongest drivers (Top20_TC; temporal pattern consistency). Results are shown for four datasets across three training configurations (epochs 100, 500, 1000).

dataset	method	runtime_s	gpu_mem_mb	cpu_rss_mb
adata_beta	Mioflow	165.72	1106.81	2111.89
adata_beta	DeepRUOT	665.74	2568.94	5213.3
adata_beta	TIGON	665.17	2437.33	5487.09
ebdata_v3	Mioflow	99.53	2412.95	6177.7
ebdata_v3	DeepRUOT	697.18	5695.58	11268
ebdata_v3	TIGON	532.97	5608.08	11330.84
MET	Mioflow	110.82	5607.66	9435.05
MET	DeepRUOT	606.07	8175.78	13935.61
MET	TIGON	561.77	8122.67	14020.09
adata_beta	GeoBridge_PCA	59.59	302.34	1302.87
ebdata_v3	GeoBridge_PCA	284.14	243.39	1354.27
MET	GeoBridge_PCA	305.59	243.14	1261.22
adata_beta	GeoBridge_HVG	99.91	2053.22	1392.71
ebdata_v3	GeoBridge_HVG	456.37	1727.69	1427.47
MET	GeoBridge_HVG	466.31	1705.67	1403.55

Supplementary Table S2 | Runtime and memory comparison across methods and datasets. All methods were evaluated on three single-cell sequencing datasets (adata_beta, ebdata_v3, MET) under their standard training budgets. GeoBridge was trained with the same number of epochs used in the held-out validation experiments (100 for adata_beta, 500 for ebdata_v3 and MET). Two input representations are reported for GeoBridge: (i) GeoBridge (50-PCA) , using the top 50 principal components, matching the dimensionality used in held-out benchmarking; and (ii) GeoBridge (2000-HVG) , using the 2,000 most variable genes without dimensionality reduction. Baseline methods were run with their originally published configurations at 50-PCA dimensionality. GPU memory reports the peak allocated memory during training (torch.cuda.max_memory_allocated); CPU memory reports the peak resident set size (RSS) of the training process. All experiments were conducted on a single NVIDIA GPU running PyTorch with CUDA.

noise	geodesic_distance_spearman	mean_geodesic_error
0	0.823000075	0.264147954
0.05	0.863886597	0.275073301
0.1	0.635229881	0.317060429
0.2	0.861069527	1.0227611
0.3	0.462022051	0.550499871

Supplementary Table S3 | Quantitative evaluation of geodesic recovery under varying spatial noise levels on the 3D Swiss roll manifold. This table quantifies the robustness of the proposed method in preserving intrinsic geometric properties when different levels of spatial noise are added to the ambient coordinates. Consistent with the visual results, the continuous temporal labels are discretized into 5 bins, inherently simulating temporal noise across all settings. **Geodesic Distance Spearman:** The Spearman rank correlation between the ground-truth analytical geodesic distances and the model-estimated distances. This metric is computed across 200 randomly sampled source-target cell pairs, measuring how well the model preserves the rank ordering of intrinsic manifold distances. **Mean Geodesic Error:** Average intrinsic geodesic distance between the recovered and true paths, measured in manifold parameter space (u , v) after nearest-neighbor projection onto the clean manifold.